Stoch Environ Res Risk Assess
DOI 10.1007/s00477-010-0385-0

ORIGINAL PAPER

Incorporation of conceptual and parametric uncertainty into radionuclide flux estimates from a fractured granite rock mass

Donald M. Reeves · Karl F. Pohlmann · Greg M. Pohll · Ming Ye · Jenny B. Chapman

Abstract Detailed numerical flow and radionuclide simulations are used to predict the flux of radionuclides from three underground nuclear tests located in the Climax granite stock on the Nevada Test Site. The numerical modeling approach consists of both a regional-scale and local-scale flow model. The regional-scale model incorporates conceptual model uncertainty through the inclusion of five models of hydrostratigraphy and five models describing recharge processes for a total of 25 hydrostratigraphic–recharge combinations. Uncertainty from each of the 25 models is propagated to the local-scale model through constant head boundary conditions that transfer hydraulic gradients and flow patterns from each of the model alternatives in the vicinity of the Climax stock, a fluid flux calibration target, and model weights that describe the plausibility of each conceptual model. The local-scale model utilizes an upscaled discrete fracture network methodology where fluid flow and radionuclides are restricted to an interconnected network of fracture zones mapped onto a continuum grid. Standard Monte Carlo techniques are used to generate 200 random fracture zone networks for each of the 25 conceptual models for a total of 5,000 local-scale flow and transport realizations. Parameters of the fracture zone networks are based on statistical analysis of site-specific fracture data, with the exclusion of fracture density, which was calibrated to match the amount of fluid flux simulated through the Climax stock by the regional-scale models. Radionuclide transport is simulated according to a random walk particle method that tracks particle trajectories through the fracture continuum flow fields according to advection, dispersion and diffusional mass exchange between fractures and matrix. The breakthrough of a conservative radionuclide with a long half-life is used to evaluate the influence of conceptual and parametric uncertainty on radionuclide mass flux estimates. The fluid flux calibration target was found to correlate with fracture density, and particle breakthroughs were generally found to increase with increases in fracture density. Boundary conditions extrapolated from the regional-scale model exerted a secondary influence on radionuclide breakthrough for models with equal fracture density. The incorporation of weights into radionuclide flux estimates resulted in both noise about the original (unweighted) mass flux curves and decreases in the variance and expected value of radionuclide mass flux.

Keywords Numerical modeling · Rock fractures · Contaminant transport · Radionuclides · Alternative model · Parametric uncertainty

D. M. Reeves (✉) · G. M. Pohll
Desert Research Institute, 2215 Raggio Parkway, Reno, NV 89512, USA
e-mail: matt.reeves@dri.edu

G. M. Pohll
e-mail: greg.pohll@dri.edu

K. F. Pohlmann · J. B. Chapman
Desert Research Institute, 755 East Flamingo Road, Las Vegas, NV 89119, USA
e-mail: karl.pohlmann@dri.edu

J. B. Chapman
e-mail: jenny.chapman@dri.edu

M. Ye
Department of Scientific Computing, Florida State University, Tallahassee, FL 32606, USA
e-mail: mye@fsu.edu

Published online: 26 March 2010

1 Introduction

The Climax stock is a fractured granitic rock mass located at the northern end of Yucca Flat in Area 15 of the Nevada Test Site (Fig. 1). Three underground nuclear detonations were conducted for weapons effects testing in the Climax stock between 1962 and 1966: Hard Hat, Pile Driver, and Tiny Tot. These three tests and the much larger Yucca Flat underground nuclear test population (739 tests) are collectively known as the Yucca Flat-Climax Mine Corrective Action Unit (CAU) (US DOE 2000a). The Yucca Flat-Climax Mine CAU encompasses a large area of approximately 500 km^2 (US DOE 2000b). A numerical flow and transport model that encompasses the entire area of the Yucca Flat-Climax Mine CAU, herein referred to as the "CAU model", is required to investigate cumulative impacts of radionuclides released from all tests within this area. The end product of the CAU model is the calculation of a contaminant boundary delineating the portion of the groundwater system that may be unsafe for domestic and municipal use for the next 1,000 years (FFACO 1996).

The inclusion of radionuclide releases from individual tests in the CAU model necessitates the development of local-scale models, herein refered to as "sub-CAU models", designed to provide detailed information, including uncertainty, on radionuclide transport from individual tests. In general, sub-CAU models are used to model a subset of tests, and results are then used to describe source releases that are not explicitly modeled from other tests located in similar hydrogeologic environments. The tests at the Climax igneous intrusive were performed in a distinctly different hydrogeologic environment than the alluvial, volcanic and carbonate rocks in Yucca Flat; hence, a separate sub-CAU model was designated to assess the potential for radionuclide migration from the Climax stock to the northern boundary of Yucca Flat. Radionuclide mass flux results from these tests will then be included in the Yucca Flat-Climax Mine CAU model.

The process of constructing a sub-CAU model of the Climax stock involved two major steps: refinement of an existing regional-scale groundwater flow model in the vicinity of the Climax stock to obtain both boundary conditions and a flux calibration target for a local-scale model, and development of a local-scale fracture continuum model to simulate fluid flow and radionuclide transport through the Climax stock (Fig. 2). The first step includes assessment of conceptual uncertainty of models describing the hydrostratigraphic framework and recharge process in the vicinity of the Climax stock. Uncertainty from each of the regional-scale conceptual models is propagated to the local-scale model through constant head boundary conditions that transfer the hydraulic gradients and flow patterns from each of the model alternatives in the vicinity of the Climax stock, a fluid flux calibration target, and conceptual model weights applied to radionuclide mass flux estimates produced by the local-scale model (Fig. 2). Moreover, radionuclide mass flux estimates are also subjected to parametric uncertainty in flow and transport properties assigned to the local-scale fracture continuum model. This study represents the first appearance in the literature of how conceptual and parametric uncertainty and their related weights influence transport estimates for a fractured rock mass. The focus of this paper is the development of a local-scale fracture continuum model for the Climax stock, propagation of conceptual model uncertainty into the local-scale model, and how conceptual and parametric uncertainty and associated weights ultimately influence final radionuclide flux estimates.

2 Climax regional-scale flow model and alternative conceptual models

The Death Valley Regional Flow System (DVRFM) model developed by the U.S. Geological Survey (Belcher 2004) provides the framework for simulating groundwater flow in the region surrounding the Climax stock, evaluating conceptual model uncertainty, and providing groundwater heads and fluxes to the local-scale Climax stock granite flow model. The DVRFM model was developed with support from the U.S. Department of Energy (DOE) to provide a common framework for investigations at the Nevada Test Site and the proposed Yucca Mountain high-level nuclear waste repository (Belcher 2004). The DVRFM model utilizes the three-dimensional groundwater flow code MODFLOW-2000 (Harbaugh et al. 2000) and was constructed from detailed characterization of hydrogeologic conditions in southwestern Nevada and the Death Valley region of California (Belcher 2004; Belcher et al. 2004).

Most aspects of the DVRFM model are preserved in the Climax Regional Flow Model (CRFM) used to simulate flow in the Climax stock and surrounding region; however, the CRFM differs in two important respects. First, the CRFM incorporates alternative models of groundwater recharge over the entire DVRFM model domain, and alternative hydrostratigraphic frameworks of the smaller area of northern Yucca Flat (solid box in Fig. 1). These alternative models address the high degree of conceptual uncertainty in these two aspects of the flow model through multiple interpretations and/or mathematical descriptions (Pohlmann et al. 2007; Ye et al. 2008). The adoption of a single model for either recharge or hydrostratigraphic framework would most likely lead to a statistical bias and underestimation of uncertainty in the final radionuclide mass flux results (Neuman 2003). Second, the horizontal mesh is highly refined from the original spacing of 1,500 m

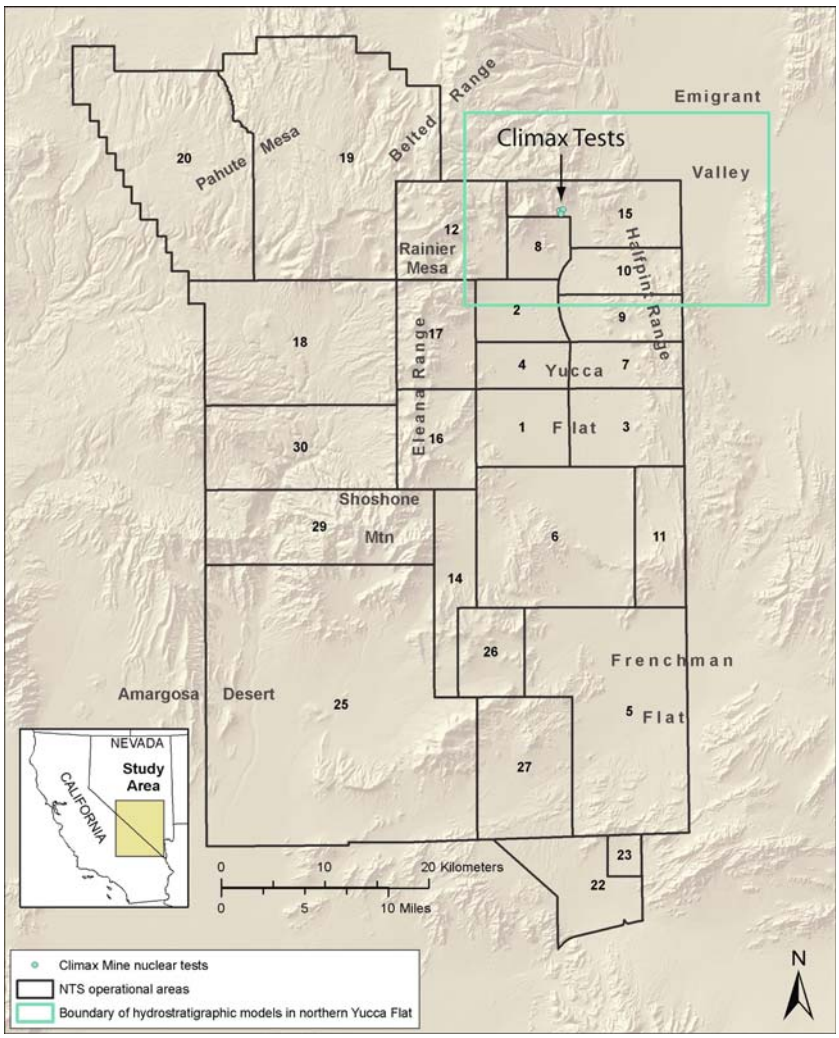

Fig. 1 Location of the Climax Mine underground nuclear tests (three clustered circles in Area 15) within the Nevada Test Site. The *solid box* represents the area updated by each conceptual geologic framework model

in the DVRFM model domain to a spacing of 250 m in northern Yucca Flat to preserve the high level of detail inherent in the hydrostratigraphic framework models (solid box in Figs. 1 and 3).

Recharge in the Climax stock area and the entire Death Valley Regional Flow System is highly uncertain. Five models incorporating different methodology and level of complexity are used to simulate the recharge process (Pohlmann et al. 2007; Ye et al. 2008). The most simple model is the modified Maxey-Eakin model (R1) which empirically relates mean annual precipitation to groundwater recharge. Watershed models are the most complex of the recharge models as they simulate various processes controlling infiltration. The two distributed parameter watershed models used to simulate net infiltration consist of alternatives of the same model. The difference between the two models is that one simulates runon-runoff processes (R2) while the other (R3) does not (Pohlmann et al. 2007; Ye et al. 2008). Recharge models with intermediate complexity consist of two chloride mass balance models that describe recharge based on estimates of chloride ion balances within hydrologic input and output components of individual basins. Two chloride mass balance methods were implemented, each with different zero-recharge masks, one for alluvium (R4) and one for both alluvium and elevation (R5). The differences in recharge masks account for uncertain conceptualizations of low-elevation recharge. The alluvium mask in model R4 eliminates recharge in areas covered by alluvium based on the study of Russell and Minor (2002). The elevation mask in model R5 further eliminates recharge in areas below an elevation of 1,237 m. This elevation corresponds to the lowest perennial spring that discharges from a perched groundwater system in the study area.

The geology in the Climax area is structurally complex and the configuration of hydrostratigraphic units is highly uncertain and open to multiple interpretations. To address this uncertainty, five hydrostratigraphic framework models (HFM) are used to represent alternative conceptualizations of the geology in the northern portion of the Yucca Flat-

Climax Mine CAU area (dashed box in Fig. 1). The first HFM (G1) was constructed by the U.S. Geologic Survey and consists of the configuration of hydrogeologic units in the DVRFM model, while the other HFMs were developed by another team of geologists for the Yucca Flat-Climax Mine CAU as part of the U.S. Department of Energy Underground Test Area program. The Underground Test Area models include a base (G2) and several alternatives (G3–G5) that address uncertainty regarding particular features of the flow system that might be important to groundwater flow and contaminant transport (Bechtel Nevada 2006). Specific alternatives include: modifications of hydrostratigraphic unit configurations according to a thrust fault (G3), a hydrologic barrier alternative where normal faulting at the east and west boundaries reduce flow through the Climax stock area (G4), and a combination of both G3 and G4 into a single model (G5). More detail on the five HFM models including cross-sections can be found in Pohlmann et al. (2007).

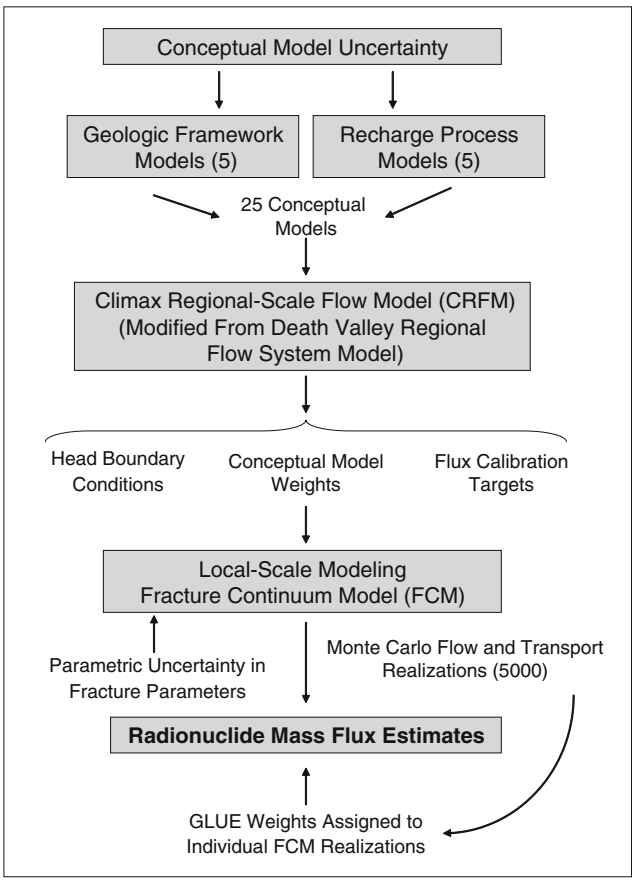

Fig. 2 Modeling schematic for the Climax sub-Corrective Action Unit model. Conceptual model uncertainty is represented by five models each of geologic framework and recharge process. The 25 conceptual models are then incorporated into the Climax Regional-Scale Flow Model (CRFM), modified from the Death Valley Regional Flow System Model. The CRFM propagates conceptual model uncertainty to the local-scale fracture continuum model (FCM) through head boundary conditions, flux calibration targets, and model weights that describe the plausibility of each conceptual model. The FCM, which incorporates uncertainty in fracture network parameters, is used to generate 200 Monte Carlo flow and radionuclide transport realizations for each of 25 conceptual models for a total of 5,000 realizations. Each FCM realization is assigned a GLUE weight based on the match between the corresponding fluid flux calibration target and total flux of the realization. Radionuclide flux estimates are then weighted according to both conceptual model and GLUE flow weights

The incorporation of five recharge and five hydrostratigraphic models into the DVRFM framework leads to a total of 25 conceptual model combinations. The plausibility (or probability) of each of these models is measured first by prior probability based on expert judgement and then by posterior model probability based on both prior probability and model calibration results. Rather than assume a non-informative equal prior, the prior model probabilities in this study (not presented) reflect the beliefs of an expert panel regarding the relative plausibility of each model according to consistency with available data and knowledge. A complete description of the expert elicitation process is beyond the scope of this paper and the reader is referred to Ye et al. (2008) for additional detail.

Posterior model probability is computed using Bayes' theorem:

$$p(M_k|\mathbf{D}) = \frac{p(\mathbf{D}|M_k)p(M_k)}{\sum_{l=1}^{K} p(\mathbf{D}|M_l)p(M_l)} \quad (1)$$

where M_k is the k-th of a total of K models ($K = 25$ in our case), $p(M_k)$ is prior probability of model M_k obtained from the expert elicitation satisfying the condition: $\sum_{k=1}^{K} p(M_k) = 1$, $p(M_k|\mathbf{D})$ is the posterior probability of model M_k conditioned on a vector of calibration data $\mathbf{D}$, and $p(\mathbf{D}|M_k)$ is model likelihood (Table 1 and Fig. 4). Model likelihood $p(\mathbf{D}|M_k)$ is based on the sum of squared weighted residuals of simulated head against 59 head observations in the northern Yucca Flat-

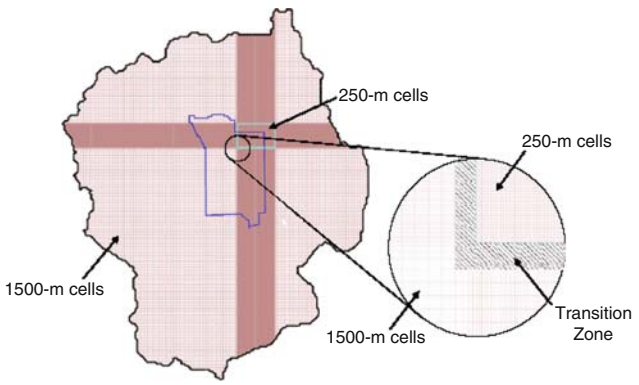

Fig. 3 Climax Regional Flow Model (CRFM) model grid (modified from the U.S. Geological Survey Death Valley Regional Flow System Model) with local refinement in the area of north Yucca Flat-Climax Stock (*box*). The outline of the Nevada Test Site is located in the center of the domain

Table 1 Values of posterior model probability, volumetric fluid flux, and corresponding fracture density for each of the 25 alternative CRFMs

Alternative CRFM (geologic framework/recharge)	Posterior model probability (%)	Volumetric flux (m^3/yr)	Fracture density (fracture cells/total cells)
G1R1	1.6	3,672,402	0.210
G1R2	2.2	2,271,897	0.175
G1R3	1.1	2,354,040	0.180
G1R4	1.4	2,252,813	0.175
G1R5	2.0	3,329,428	0.220
G2R1	6.3	6,002,826	0.600
G2R2	13.2	1,363,970	0.225
G2R3	6.5	1,220,893	0.200
G2R4	6.0	3,472,896	0.425
G2R5	7.4	3,483,820	0.425
G3R1	5.1	3,601,819	0.475
G3R2	14.0	757,169	0.138
G3R3	2.9	706,644	0.138
G3R4	4.3	1,798,069	0.275
G3R5	8.8	2,291,447	0.325
G4R1	1.2	7,025,040	0.625
G4R2	3.3	1,351,006	0.185
G4R3	1.9	1,409,483	0.200
G4R4	1.7	1,792,410	0.250
G4R5	3.5	3,751,154	0.450
G5R1	9.6	4,039,050	0.575
G5R2	1.9	1,031,675	0.225
G5R3	1.8	1,677,226	0.325
G5R4	1.0	1,280,366	0.263
G5R5	1.9	2,633,991	0.450

Climax area generated during the calibration of each conceptual model. The generalized likelihood uncertainty estimation (GLUE) technique (Beven and Binley 1992) is used to compute model likelihood according to the inverse of the sum of square residuals for each of the calibrated conceptual models (more detail on the GLUE technique is presented in Sect. 3.2). The GLUE technique in this study was favored over information criterion based approaches (e.g., Akaike 1974; Hurvich and Tsai 1989; Schwarz 1978; Kashyap 1982) for model averaging since these approaches were found to limit conceptual uncertainty to only two models (Ye et al. 2010). The geologic and hydraulic data in the vicinity of northern Yucca Flat-Climax are too sparse to justify the exclusion of the other 23 models, and the exclusion of these models would lead to an under-estimation of conceptual model uncertainty. The GLUE technique on the other hand allows for the inclusion of all 25 models by more evenly distributing values of model likelihood. It is worth mentioning that the GLUE technique, unlike information criterion based approaches, is solely based on the goodness-of-fit obtained during calibration (sum of squared weighted residuals) and does not take into account model complexity.

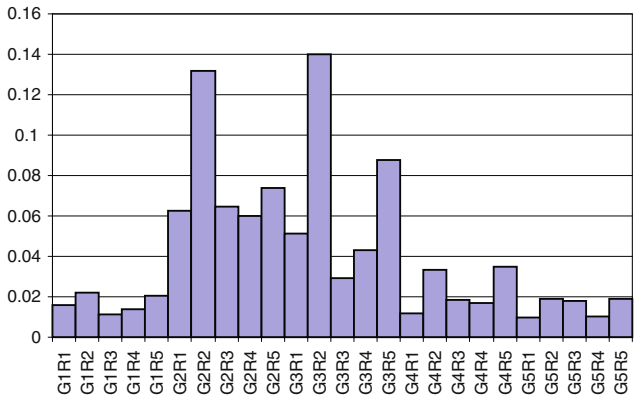

Fig. 4 Plot of posterior model probability for all 25 geologic framework and recharge combinations. Note that the two most dominant models, G2R2 and G3R2, combined only contain 27% of the total model weight, and that 75% of the total model weight is contained within geologic framework models G2 and G3

Analysis of posterior model probabilities yields several conclusions. First, a single dominant model was not identified. The two most plausible models are G2R2 and G3R2 with (only) a combined 27% of the total model weight (Table 1 and Fig. 4). Second, though none of the individual

models are dominant, the geologic framework models, specifically G2 and G3 that combined account for nearly 75% of the total model weight, have more influence on posterior model probabilities than recharge models. This should not be surprising because posterior probability is heavily influenced by model likelihood values determined during model calibration, and the geologic framework exerts more control on flow than recharge (i.e., recharge variations can be accommodated to some extent by the range in hydraulic conductivity values assigned to different hydrostratigraphic units). The broad distribution of posterior probability across all alternative conceptual models influence radionuclide flux estimates, yet these flux estimates will clearly be most heavily influenced by geologic framework models G2 and G3.

3 Simulation of flow and radionuclide transport in the Climax stock

The Climax stock is a fractured intrusive body consisting of low-permeability Cretaceous-age monzogranite and granodiorite. The stock is nearly circular at depth, covering an area of approximately 200 km^2 and extending to a depth of 7.5 km. The three underground nuclear tests at Climax were conducted near or just below the water table. To maintain consistency with the Underground Test Area protocol, the tests and their radionuclide source term were projected to the saturated zone due to their close proximity to the water table and to avoid the complexity of radionuclide migration in the vadose zone. This is a conservative measure with respect to the downstream migration of radionuclides.

Local-scale modeling efforts consider the saturated portion of the Climax stock exclusively and are based on the discrete fracture network (DFN) conceptual model where rock fractures embedded within a low permeability matrix provide primary pathways for fluid flow and radionuclide migration. Thus, according to this conceptual model, potential radionuclide migration from the Hard Hat, Pile Driver and Tiny Tot underground tests is controlled by physical and hydraulic properties of interconnected fracture networks. This conceptual model is supported by the degree of fracturing observed at the Climax stock and the large contrasts between field-scale hydraulic conductivity estimates (10^{-7} to 10^{-10} m/s) and laboratory hydraulic conductivity estimates of unfractured rock cores (10^{-12} to 10^{-15} m/s) (Murray 1980, 1981).

3.1 Fracture continuum model

The scale of the Climax stock (several kilometers) as compared to the scale of individual fractures exceeds the computational capacity of three-dimensional DFN models. Instead, a fracture zone continuum approach, which establishes a hierarchy between model cells by assigning properties of either discrete fracture zones or an upscaled rock matrix, is used to simulate steady-state, three-dimensional groundwater flow through the Climax stock. The fracture continuum model (FCM) domain is based on the saturated configuration of the Climax stock, excluding any surrounding geologic units in northern Yucca Flat. The local-scale model extends from 3,000 m in the *x*-direction and 2,250 m in the *y*-direction (Fig. 5). In the vertical direction, the model extends from 1,155 m (the highest elevation of the DVRFM water table within the local-scale model domain) to mean sea level. A constant flux is applied to the upper FCM model boundary to represent recharge to the water table, and the lower model boundary is no flow. Annual recharge flux estimates in the area of the local-scale FCM domain range between 2.0 and 9.9 mm/yr

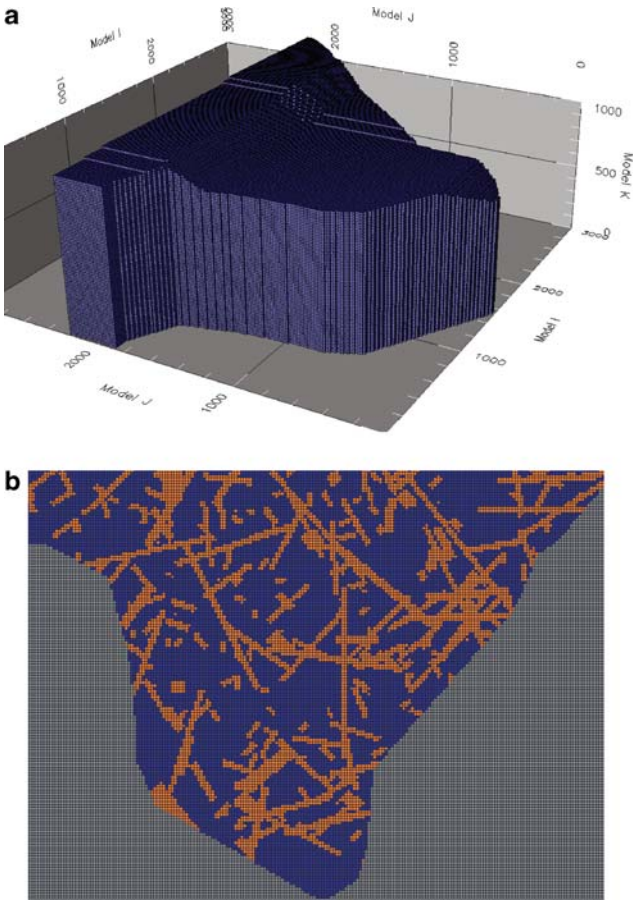

Fig. 5 **a** Northeast view of the local-scale fracture continuum model, along with **b** 2D slice showing fracture zone network at a density of 0.30 at model layer 15. Fracture zone thickness is a function of dip (i.e., gently dipping zones appear thicker than steeply dipping zones). Fracture zones that appear unconnected in the figure may be connected in 3D. The model is 3 km in the *x*-direction and 2.25 km in the *y*-direction, with a cell size of 15 m per side

Table 2 Values of recharge flux for each alternative conceptual model in the local-scale fracture continuum model

Recharge model	Recharge rate (mm/yr)	Recharge rate (m^3/yr)
Modified Maxey-Eakin	6.8	24,655
Net infiltration I	9.9	36,262
Net infiltration II	2.0	7,173
Chloride mass-balance I	4.8	17,679
Chloride mass-balance II	4.8	17,679

Table 3 Statistics of fracture sets in the SFT-C database

	Set1	Set2	Set3	Set4	Set5	Set6	Set7
Prior probability	0.03	0.13	0.10	0.14	0.13	0.32	0.15
Mean strike	125	317	360	321	289	48	N/A
Mean dip	19	25	85	83	82	80	N/A
Dispersion (κ)	65	37	33	24	23	18	N/A

(Table 2). The lack of an alluvial mask in the area of the CRFM containing the local-scale FCM model domain yields identical recharge estimates of 4.8 mm/yr for both chloride mass-balance models. In general, recharge applied to the local-scale FCM accounts for only 1% of the total volumetric flux through the granite rock mass. All lateral FCM boundaries are constant head using values interpolated from each CRFM. A finite-difference groundwater flow code, MODFLOW-2000 (Harbaugh et al. 2000), solves the steady-state groundwater flow equation for both fracture networks and rock matrix. A subset of 200 fracture network zone realizations is generated for each of the 25 CRFM using standard Monte Carlo techniques to adequately sample fracture network parameters while staying within computational constraints.

Fracture zone networks are randomly generated for seven fracture sets according to a compound Poisson process for fracture location, a Fisher distribution for variability about mean fracture set orientations, a truncated Pareto distribution for fracture length, a lognormal distribution for fracture hydraulic conductivity, and an algorithm, based on the ratio between fracture-occupied cells and total cells in the model domain, to control fracture density (Appendix). These random fracture zone networks are then mapped onto a continuum grid with a constant cell size of 15 m × 15 m × 15 m (Fig. 5). A novel mapping algorithm, based on the equation of a plane, is used to accurately map discrete fractures (as fracture zones) of any strike and dip orientation as two-dimensional planar features within a three-dimensional finite-difference model domain. The use of a finite-difference grid to simulate discharge in a fracture that is not aligned with the grid requires an adjustment for longer flow paths (Botros et al. 2008; Reeves et al. 2008a):

$$K_{\text{MODFLOW}} = K_{\text{fracture}} \cdot [\sin|\theta| + \cos|\theta|] \quad (2)$$

where the correction factor $\sin|\theta| + \cos|\theta|$ ensures a correct amount of flux through grid mapped fractures oriented at angle θ to the grid. Fractures mapped onto the grid are randomly assigned values of hydraulic conductivity according to one of the two lognormal distributions described in the Appendix. Cells unoccupied by fractures represent an upscaled matrix with a small degree of background fracturing and are assigned a hydraulic conductivity value of 10^{-10} m/s. Interestingly, this upscaled matrix hydraulic conductivity value is very close to the mean hydraulic conductivity value used in the stochastic continuum model of Hendricks Franssen and Gómez-Hernández (2002) to represent an upscaled granite rock matrix with background fracturing.

3.2 Flow model calibration and weighting

There are no reliable head measurements in the Climax stock; therefore, head values could not be used as calibration targets. Instead, each of the 25 CRFMs was used to provide both boundary conditions and target volumetric flux values for each 200 realization subset of the 5,000 total FCM flow realizations. The target volumetric flux is defined as total annual flow [m^3/yr] simulated through cells of the CRFM grid that correspond to the local-scale FCM domain. Calibration of the fracture continuum realizations to all CRFMs was further complicated by the approximate order-of-magnitude difference in the 25 CRFM volumetric flux values (706,644 to 7,025,040 m^3/yr) (Table 1).

The calibration of fracture network parameters to the large range in volumetric flux values for the 25 conceptual models could possibly occur by either adjusting mean hydraulic conductivity or fracture density. Of these two parameters, fracture density was deemed more uncertain as the frequency of flowing fractures, defined as the interconnected network of fractures responsible for flow, is completely unknown. While fracture hydraulic conductivity is also uncertain, Murray (1980, 1981) suggested a range of fracture hydraulic conductivity values between 10^{-7} to 10^{-10} m/s based on bulk hydraulic conductivity values obtained from hydraulic tests in the Climax stock. The calibration of volumetric flux to fracture density implies that each CRFM, through its flux value, represents a different level of network connectivity as flow is

proportional to fracture connectivity (assuming the distribution hydraulic conductivity is held equal), and increases in fracture density in the fracture zone generation code lead to greater levels of network connectivity.

Calibration of volumetric flux to fracture density using least-square methods to minimize volumetric flux residuals (e.g., Doherty 2000) proved unsuccessful due to objective functions with several local minima, and the finding that volumetric flux values through individual network realizations having the same density can vary over several orders of magnitude. The variability in flux values for randomly generated networks with identical density values is attributed to the degree of network connectivity and the hydraulic conductivity values assigned to individual fracture segments. As an alternative to inverse methods, FCM calibration was considered to be achieved when the geometric mean of simulated flow for all 200 realizations is within $\pm$ 5% of the CRFM target flux. Mean fracture set hydraulic conductivity values of 10^{-7} and 10^{-8} m/s were found to simulate the range in CRFM volumetric flux by producing backbones above the percolation threshold at lower volumetric flux values (necessary for network flow), yet only occupy approximately half of the model grid at higher volumetric flux values (necessary for the implementation of the fracture continuum method). A trial-and-error process was used to determine values of fracture density.

In a standard Monte Carlo simulation, all of these realizations, regardless of flux values, would have equal weight. However, given the extreme variability in flux across all realizations, it is reasonable to assume that flow realizations that more closely match the target flux value for a CRFM should receive more weight than flow realizations that show a poor match to the given target flux. Since the calibration of flux was not achieved from a least-square or maximum likelihood perspective, Bayesian model averaging techniques (e.g., Neuman 2003; Vrugt et al. 2008) were not used. Instead, a generalized likelihood uncertainty estimate (GLUE) technique (Beven and Binley 1992) is used to assign weights to each of the 200 individual flow realization subsets for a given CRFM according to:

$$L(\mathbf{F}|\boldsymbol{\theta}_\mathbf{i}|) = \left(\frac{1}{E_i}\right)^N \tag{3}$$

where $L(\mathbf{F}|\boldsymbol{\theta}_\mathbf{i}|)$ is the likelihood of the vector of simulated flux values for the local-scale FC realizations, $\mathbf{F}$, given the parameter set, $\boldsymbol{\theta}$. E_i is an objective function and N is a likelihood shape factor that can range from zero to infinity. By assuming a weak correlation between flux in each CRFM and the corresponding FCM realizations, the objective function can be defined as: $E_i = (Flux_i - Flux_t)^2$, where $Flux_i$ are flux values for FCM realizations with index i, and $Flux_t$ is the target flux value for the corresponding CRFM. The selection of N is central to the GLUE weighting method. A value of zero describes a standard Monte Carlo realization where all realizations have equal weight. As N increases from zero toward infinity, probability is shifted towards the realizations that best match the objective function. Traditionally a value of 1 is used for N, but the shape factor can also be chosen by the user (Beven and Binley 1992).

Flux values in the fracture zone networks are constrained only by the range and distribution of the network parameters and the constant head boundary conditions from the corresponding CRFM. As a consequence, the degree of variability in values of flux for these networks is much greater than would be expected if regional flow constraints were placed on the local-scale FCM. To address variability in volumetric flux through the Climax stock while adhering to regional flow constraints, 200 regional-scale flow realizations were generated for each CRFM. The distribution of flux values from the regional-scale realizations, where parametric uncertainty is addressed by using a covariance matrix for each of the 25 calibrated regional models (i.e., for a given parameter, its calibrated value is the mean and the deviation about the mean is described by its covariance), are thought to better reflect the variability in flow that is possible for the Climax stock. These regional-scale CRFM flux values are used in conjunction with flux values from the local-scale FCM to define N.

Values of flux from the regional-scale realizations are sorted and ranked to compute an empirical cumulative distribution function (CDF). Next, given an arbitrary value of N, an empirical CDF for the local-scale FCM flow weights, $L(\mathbf{F}|\boldsymbol{\theta}_\mathbf{i}|)$ is computed according to (3). Flux values corresponding to the 95% confidence intervals, 0.025 and 0.975, are compared for both the regional-scale and local-scale models. The value of N, which controls the distribution of weights for the local-scale model, is then changed until the difference in flux values corresponding to the lower and upper 95% confidence intervals is minimized (Franks et al. 1999; Beven and Freer 2001). By following this procedure for all 25 CRFMs, N was found to range between 0.44 and 1.0. The mean (and median) of the distribution of N is 0.69. The use of this value shifts probability weight to realizations that best match the target flux value. Figure 6 shows the influence of the cumulative distribution of model weights based on flux for one of the 200 realization subsets.

3.3 Model averaging

Final weights for each FCM flow realization are a combination of the GLUE flow weights assigned to the 200-

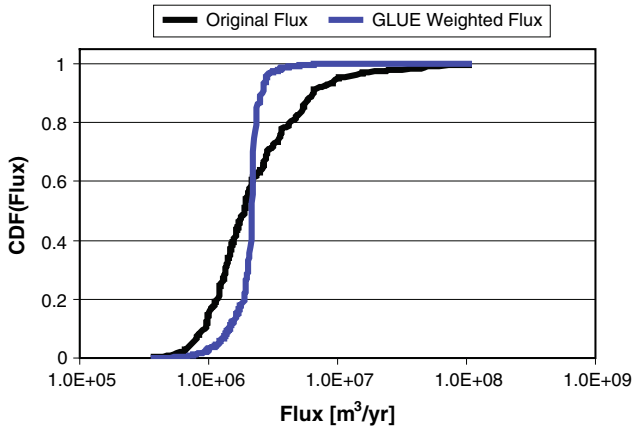

Fig. 6 Cumulative distribution of weights for FCM realizations corresponding to the G1R2 boundary conditions and flux target before and after the GLUE weighting procedure. A similar trend in GLUE weights was observed for all of the other realization subsets. Note that the GLUE weighting procedure preferentially weights realizations that more closely match the target flux value (2.2×10^6 m^3/yr) based on *N*. All other 200 realization subsets exhibit similar trends

realization FCM subset, with the model weight (posterior probability) assigned to the CRFM that provides the boundary conditions and flux calibration target. Final weights are then used to scale the simulated radionuclide flux estimates according to each flow realization and the CRFM it represents. A model averaging method is used to compute the posterior mean:

$$E[\triangle|\mathbf{D}] = \sum_{k=1}^{25} E[\triangle|\mathbf{D}, \mu_k] w(\mu_k|\mathbf{D}) \quad (4)$$

where $\triangle$ is radionuclide mass flux, $\mathbf{D}$ is a discrete data set of 59 hydraulic head observations, μ is the geologic-recharge model with index k, $w(\mu_k|\mathbf{D})$ represents weights assigned to each conceptual model μ_k, and

$$E[\triangle|\mathbf{D}, \mu_k] = \frac{1}{N} \sum_{i=1}^{200} [\triangle|\mathbf{D}, \theta_i] w(\theta_i|\mathbf{D}) \quad (5)$$

where θ is a FCM realization with index i and $w(\theta_i|\mathbf{D})$ represents GLUE flow weights assigned to each FCM subset. By combining Eqs. 4 and 5, the final weights are described by:

$$E[\triangle|\mathbf{D}] = \frac{1}{N} \sum_{k=1}^{25} \sum_{i=1}^{200} [\triangle|\mathbf{D}, \mu_k, \theta_i] w(\mu_k|\mathbf{D}) w(\theta_i|\mathbf{D}) \quad (6)$$

where the final weights $E[\triangle|\mathbf{D}]$ are a linear combination of the probability assigned to the CRFM models $w(\mu_k|\mathbf{D})$ and the GLUE flow weights assigned to each FCM subset $w(\theta_i|\mathbf{D})$. The application of the final weights to the radionuclide mass flux calculations is discussed Sect. 4.

3.4 Simulation of radionuclide transport

The FCM flow fields of the Climax stock preserve the degree of heterogeneity and anisotropy that fracture networks impart on a groundwater flow system. By simulating particle trajectories through the fracture zone network flow solutions, particles sample a wide variety of fracture zone lengths, orientations and velocities before reaching model boundaries. Preferential transport of particles through interconnected fracture zones of the hydraulic backbone controls radionuclide breakthrough at model boundaries.

The simulation of radionuclide trajectories through the Climax stock FCM flow fields is based on a random-walk particle code, Ptrack (Pohlmann et al. 2004, 2007). Ptrack simulates advective and dispersive particle motion according to the random walk particle method of LaBolle et al. (1996, 2000). Time steps are computed from velocity and longitudinal dispersivity values to ensure that particles within fractures do not overshoot fracture cells in a given jump and enter low-permeability cells of the simulated matrix. The computation of dispersion coefficients at an intermediate location between particle jumps avoids potential gradient effects for cells that have sharp contrasts in advective velocity and/or porosity. Macrodispersion of radionuclides arises from the geometry of the FCM networks (Reeves et al. 2008b, c), while within-fracture dispersion is simulated by a local-scale anisotropic Gaussian dispersion tensor with values of 1.5 m (10% of the cell size) and 0.15 (1% of the cell size) for longitudinal and transverse dispersivity, respectively. The trilinear interpolation scheme of the particle tracking code results in a variable velocity field within each fracture, where particle velocity is dependent on the position of each particle relative to the matrix or other low velocity cells. The application of a very small component of transverse dispersion randomizes particle sampling of streamlines and velocities present within a given fracture zone (i.e., transverse dispersion promotes flow path mixing within fracture zones). Sensitivity of transport results to the local dispersivity tensor was not investigated.

A random walk particle transfer approach, originally formulated by Liu et al. (2000) and modified by Hassan and Mohamed (2003), is used to describe the diffusion of particles from rock fractures into matrix blocks of finite size and, once in the matrix, the diffusion of particles back to the rock fractures. This algorithm is based on transfer probabilities that control the movement of particles between rock fractures and matrix blocks. Transition times for the RWPT approach are based on an idealized geometry of rectangular matrix blocks bounded by parallel fractures. Transfer probabilities are dependent on parameters such as a constant diffusion coefficient, average fracture spacing and aperture, matrix porosity, retardation coefficients for

the matrix and fractures, and advection in the matrix and fractures (refer to Hassan and Mohamed (2003) for more detail). An average fracture spacing of 6 m, based on the assumption that only 10% of the total fracture population contributes to flow (Dershowitz et al. 2000), is used to parameterize the random walk particle transfer algorithm. A constant aperture value corresponding to the geometric mean aperture from the SFT-C database and a constant diffusion coefficient of 1.0×10^{-6} m^2/d, representative of a generic radionuclide, is used for all transport simulations.

Radionuclide particles per realization are randomly distributed over permeability disks incorporated into the FCM permeability fields located at the top of the model domain (water table), defined as two-dimensional radial features with hydraulic conductivity and porosity values of 10^{-8} m/s and 0.20 (Fig. 7a). These features are used as an alternative to spherical damage zones due to the large degree of uncertainty regarding the elevation of the water table relative to the elevation of the three underground tests. Recall that a conservative assumption was made to project the radionuclides downward to the water table. The radius of each permeability disk is a function of the extent of shock fracturing, which is proportional to the announced yield range of each test. The porosity of the permeability disks (0.20) is representative of high-porosity rubble material. The total transport simulation time is 1,000 years.

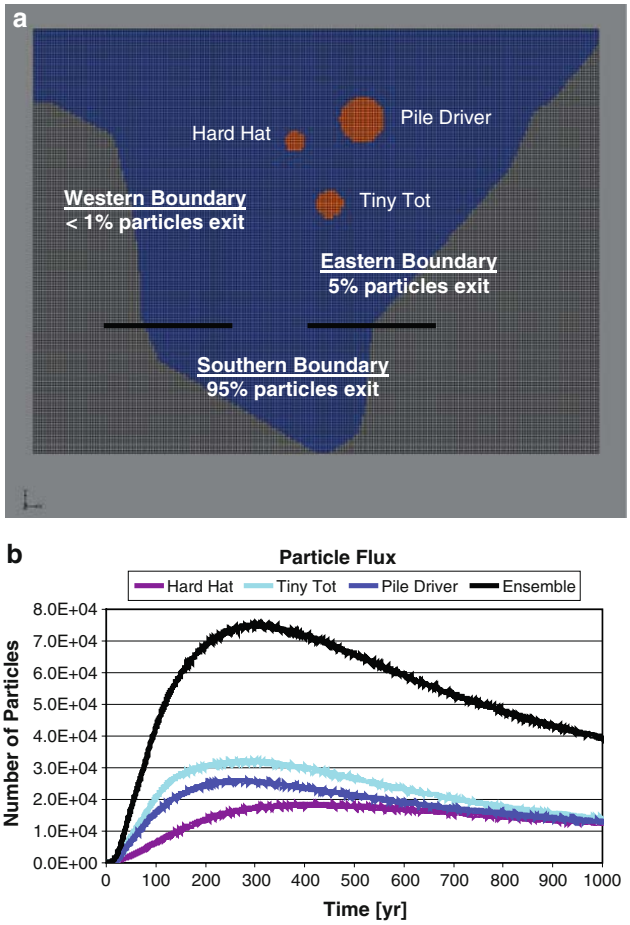

Fig. 7 **a** Location of eastern, western, and southern model boundaries along with percentage of particles exiting each boundary and **b** particle flux times to model boundary for each source origin along with the ensemble trend for all 5,000 realizations. The *circular areas* in (**a**) represent the permeability disk assigned to each underground test (proportional to announced yield range), and *thick horizontal lines* delineate the southern boundary

4 Radionuclide breakthrough and influence of conceptual and parametric model uncertainty

To demonstrate the influence of conceptual and parametric uncertainty on radionuclide flux estimates, we provide details of radionuclide flux for ^{14}C, a radionuclide with a long half-life ($t_{1/2}$=5,730 yr) assumed here to transport conservatively (non-sorbing). The use of a conservative radionuclide ensures that the breakthrough curves reflect the flow and transport properties of the fracture zone networks. The long half-life of ^{14}C is desirable as the shape of the breakthrough curves are not dramatically altered at late times from mass loss. It should be noted that ^{14}C may be more complex than simulated here, including gas phase transport and reactions with minerals, but compared to many other long-lived radionuclides in the nuclear source term, it is relatively conservative. More conservative radionuclides such as ^{3}H or ^{85}Kr could have been used in this paper, but the shorter half-lives of these radionuclides distort the late time breakthroughs.

The determination of radionuclide flux from the Climax stock starts with the computation of particle flux to the boundaries of the local-scale FCM. Since Ptrack simulates particle transport for all sources starting at $t = 0$ (i.e., time of the Hard Hat test), particle exit times for the Tiny Tot and Pile Driver underground tests are increased (shifted) by 5.34 and 6.30 years, respectively. Exit times for each radionuclide particle for each of the 5,000 transport realizations are then binned into one-year intervals over a 1,000-year time span for each source origin. Each particle from a given realization and time interval is assigned a molar mass specific to ^{14}C, where particle mass is equal to the total source term mass according to a particle's origin (i.e., Hard Hat, Tiny Tot, or Pile Driver) divided by the total number of particles used in the transport simulations (30,000 per realization). This mass is then rescaled by an algorithm based on Faure (1977) to compute radionuclide decay. After the rescaling process, values of ^{14}C mass flux from each test are combined to form an ensemble mass flux. Final weights, as described in Sect. 3.3, are applied to the values of ensemble mass flux for each realization at every time step and an empirical cumulative distribution

function (CDF) is computed from the final weights. Values of ensemble mass flux corresponding to the median and the upper and lower 95% confidence intervals (U95 and L95) are then determined from the empirical CDF for each time step. Mean mass flux for a given time interval is the product sum of mass flux values and their corresponding weights for all 5,000 FCM realizations.

Particle breakthroughs at model boundaries (the margins of the Climax stock) for all 5,000 transport simulations are presented in Fig. 7. Approximately one-third of the ^{14}C particles exit the model domain within the total transport time of 1,000 years. Of the particles that leave the model domain, 26% originate from the Hard Hat test, 41% originate from the Tiny Tot test, and 33% originate from the Pile Driver test (Fig. 7b). Differences in particle breakthrough are attributed to test location relative to the southern boundary (transport distance) and size of the permeability disks (larger permeability disks have a greater chance of intersection by the hydraulic backbone). Approximately 95% of all particles exit through the southern model boundary (Fig. 7a). This demonstrates that the general flow direction of northeast to southwest flow through the Climax stock (Murray 1981) is preserved in the local-scale FCM despite the randomness of the fracture zone networks. Particle flux at the local-scale FCM boundaries for the Hard Hat, Tiny Tot, and Pile Driver tests peaks at 414, 276, and 263 years, respectively (this is without consideration of radioactive decay) (Fig. 7b). The peak arrival time for the ensemble of the three tests occurs at 307 years.

The raw (i.e., unprocessed) particle flux times to model domain boundaries (Fig. 7b) incorporate conceptual model uncertainty propagated to local-scale FCM realizations through constant head boundary conditions, a fluid flux calibration target, and model weights that describe the plausibility of each model. Parametric uncertainty in the local-scale flow model is addressed by fracture zone networks with random zone placement, orientation, length and hydraulic conductivity. Further parametric uncertainty is introduced during the simulation of transport including an anisotropic within-fracture dispersion tensor, fracture zone porosity (correlated with fracture K), and the random walk particle transfer approach used to simulate the motion of radionuclide particles between fractures and the rock matrix. Despite the inclusion of parametric uncertainty, fracture density—obtained through calibration to the volumetric flux target for each CRFM—is the only parameter that differs between all 200 FCM realization subsets for each of the 25 conceptual models. All other statistical properties of the FCM are held equal.

While it is not possible to completely decouple the influence of conceptual and parametric uncertainty on ensemble radionuclide flux estimates, insight into the influences of both types of uncertainty can be gained by computing total particle breakthrough over the 1,000 year simulation period for each of the 25 conceptual models prior to and after application of conceptual model weights (Fig. 8). Upon inspection of the unweighted particle breakthroughs, it is apparent that total particle breakthrough generally increases with fracture density (note that the conceptual models in Fig. 8 are listed in order of increasing density). Deviations in the trend are caused by the boundary conditions from each CRFM that define the hydraulic gradient across the Climax stock. For example, models G3R2 and G3R3 have the same fracture density and individual realizations have identical fracture zone networks (random seeds used in the fracture zone network generation code are related to the realization number), yet the G3R2 boundary conditions result in 7 times greater breakthrough than observed for G3R3. The application of model weights dramatically changes the magnitude of particle breakthrough and somewhat weakens the trend of higher particle breakthrough with greater fracture density. A greater than 50% change in magnitude occurs for 18 of the 25 conceptual models. The most dramatic changes are observed for models G3R5, G2R2, and G3R2 for which the application of model weights changes the magnitude of particle breakthrough by 121, 233 and 235%, respectively.

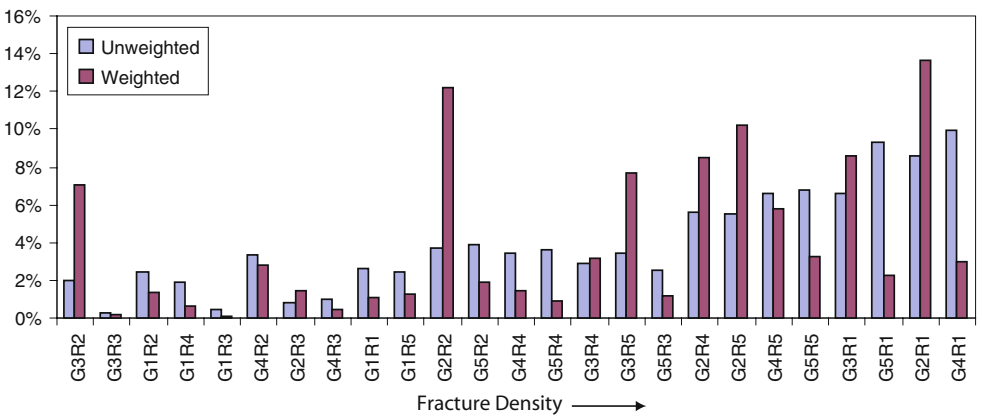

Fig. 8 Percentage of total particle breakthrough over the 1,000 year simulation period for each conceptual model prior to (unweighted) and after (weighted) application of conceptual model weights. Conceptual models are listed in order of lowest to highest fracture density

The impacts of incorporating both conceptual model and GLUE weights, assigned to each FCM realization based on the match to the CRFM volumetric flux calibration target, on the particle mass flux curves for ^{14}C in an ensemble sense are illustrated in Fig. 9. Figure 9a consists of equally-weighted realizations according to particle flux arrival times to model boundaries, i.e., a straight Monte Carlo simulation without preferential weighting. The only difference between the ensemble curve in Fig. 7b and the curve shown in Fig. 9a is a rescaling of the ^{14}C source mass according to Bowen et al. (2001), and subsequent mass loss over time through radioactive decay. Note that the lower 95% ^{14}C mass flux is zero, implying that several FCM realizations do not contribute to particle breakthrough and that the 95% confidence interval ranges between 0 and the upper 95% interval [moles/yr].

The application of model weights to the radionuclide mass flux curves in Fig. 9a does not dramatically change the radionuclide mass flux estimates, as only slight changes are observed in the mean and median flux estimates. The upper 95% mass flux curve slightly lowers from a peak of 5.8×10^{-5} to 5.0×10^{-5} mol/yr of ^{14}C, which corresponds to a decrease in variance of the mean radionuclide flux through the introduction of model weights. Additionally, the inclusion of model weights into the radionuclide mass flux curves in Fig. 9b result in slightly more irregular profiles along the mass breakthrough curves in Fig. 9a. The irregular profiles in Fig. 9b reflect the preferential weighting of radionuclide particles at model boundaries, where weights applied to the radionuclide particles are derived from each regional-scale CRFM (refer to Sect. 2). The relative insensitivity of the radionuclide mass flux curves to model weights is reflected by the relatively even spread of posterior model probability. Model weights would have a much greater impact on radionuclide flux estimates if the distribution of model weight was more concentrated on a few models. Recall that the relatively even distribution of posterior probability is a reflection of sparseness of geologic and hydraulic data in the vicinity of the model domain.

The incorporation of GLUE weights to the mass flux curves shown in Fig. 9a result in much more erratic profiles (Fig. 9c) than caused by the model weights (Fig. 9b). The noisy quality of the GLUE-weighted curves reflects values of weights assigned to particles from individual realizations—recall that GLUE weights are based on matching volumetric flux values for individual FCM realizations to a target volumetric flux for a corresponding conceptual model (Table 1 and Fig. 4). Given that the majority of fluid flow occurs through interconnected fracture zones of the hydraulic backbone, the volumetric flux values are an indirect measure of fracture zone connectivity. Thus, the GLUE weights indirectly reflect the degree of network

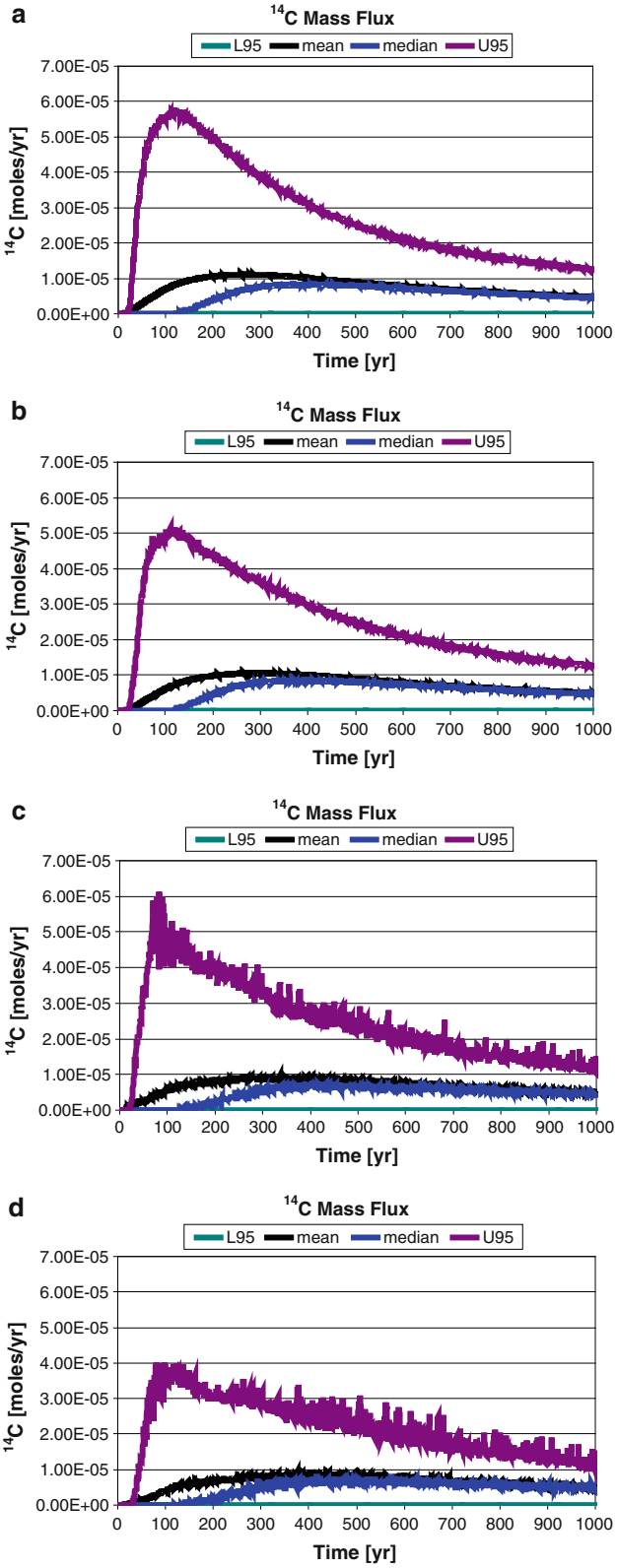

Fig. 9 **a** Mass flux for ^{14}C based on a straight Monte Carlo simulation where all realizations are equally weighted, **b** mass flux after application of model weights, **c** mass flux after application of GLUE weights, and **d** mass flux after application of both model and GLUE weights

connectivity which represents parametric uncertainty produced by random fracture zone placement, orientation, length and hydraulic conductivity. Despite the noise, the GLUE weighted mass flux curves (Fig. 9c) follow the same general trend as the equally weighted Monte Carlo mass flux curves (Fig. 9a).

The final weights assigned to the mass flux curves are a combination of both model and GLUE weights (refer to Sect. 3.3). The multiplication of these weights increases the amplitude of the noise as the final radionuclide mass flux curves exhibit the most erratic profiles (Fig. 9d). The magnitude of the mass flux curves subject to the final weights shows a more dramatic decrease in peak magnitude for all confidence intervals, except for the lower 95% confidence interval which equals zero for all cases. The upper 95% confidence interval decreases from approximately 5.8×10^{-5} mol/yr of ^{14}C for the equally weighted curves in Fig. 9a to 3.8×10^{-5} mol/yr. The combined model weights appear to exert the most influence on the magnitude of early breakthroughs. The greatest decrease in the estimates of mass flux, particulary the variance, is to be expected after the application of the final weights since these weights preferentially weight particle breakthroughs from conceptual models that are most plausible and FCM realizations that best match the volumetric flux calibration target.

5 Conclusions

Detailed numerical flow and transport simulations are used to support CAU modeling efforts by predicting the flux of radionuclides from three underground nuclear tests conducted in a fractured granite rock mass on the Nevada Test Site. A regional-scale model incorporates conceptual model uncertainty through the inclusion of five models of hydrostratigraphy and five models describing recharge prcoesses for a total of 25 hydrostratigraphic–recharge combinations. Uncertainty from each of the 25 models is propagated to the local-scale model through boundary conditions, a fluid flux calibration target, and model weights that describe the plausibility of each conceptual model. Radionuclide transport estimates for the Climax stock are based on a local-scale fracture continuum model parameterized according to analysis of site-specific rock fracture data, and calibration of fracture density to volumetric flux. Each local-scale FCM is assigned a GLUE weight according to the match between flux of the realization and the target volumetric flux.

The flux calibration target was found to correlate with fracture density, and particle breakthroughs were generally found to increase with increases in fracture density. Boundary conditions extrapolated from the conceptual models exerted a secondary influence on radionuclide breakthrough for models with equal fracture density. The incorporation of model and GLUE weights results in both noise about the original (unweighted) mass flux curves and decreases in the variance and expected value of radionuclide mass flux. The moderate insensitivity of the radionuclide flux estimates to the final weights is based on the more or less even distribution of posterior model probability assigned to each of the conceptual models due to sparse geologic and hydraulic data. It is anticipated the concentration of model weight around only two models would dramatically affect the radionuclide mass flux estimates after weighting of particle breakthroughs produced by each model.

Acknowledgements This research was supported by the U.S. Department of Energy, National Nuclear Security Administration Nevada Site Office under Contract DE-AC52-00NV13609 with the Desert Research Institute. Special thanks goes to the guest editor Dr. Yu-Feng Lin and Drs. Yonas Demissi, Abhishek Singh and Andrew F.B. Tompson for constructive comments that greatly improved the quality of the manuscript.

Appendix: Fracture characterization

Numerical modeling of fluid flow in fracture dominated subsurface flow regimes requires statistical analysis of fracture data for the determination of fracture properties, such as fracture sets and their mean orientation, length, spacing and distribution, density, and permeability of individual fractures or zones (e.g., Munier 2004; Reeves et al. 2008a). Fracture characterization at the Climax stock is based on the Spent Fuel Test—Climax (SFT-C) Geologic Structure Database (Yow 1984) that consists of data describing joints, faults and shear zones (sample population $n = 2,591$) that were collected during fracture mapping efforts in tunnel drifts constructed for the Climax Spent Fuel Test.

Fracture set orientation

Analysis of fracture orientation statistics, according to standard spherical statistical tests (Mardia and Jupp 2000), reveals a total of seven fracture sets (Table 3 and Fig. 10). Of the seven fracture sets, Sets 1 through 6 fit a Fisher distribution (Fisher 1953):

$$f(x) = \frac{\kappa \cdot \sin(x) \cdot e^{\kappa \cdot \cos(x)}}{e^{\kappa} - e^{-\kappa}} \tag{7}$$

where the divergence, x (degrees), from a mean orientation vector is symmetrically distributed $\left(-\frac{\pi}{2} \leq x \leq \frac{\pi}{2}\right)$ according to a constant dispersion parameter, κ. The Fisher distribution is a special case of the Von Mises distribution, and is similar to a normal distribution for spherical data (Mardia and Jupp 2000). The extent to which individual

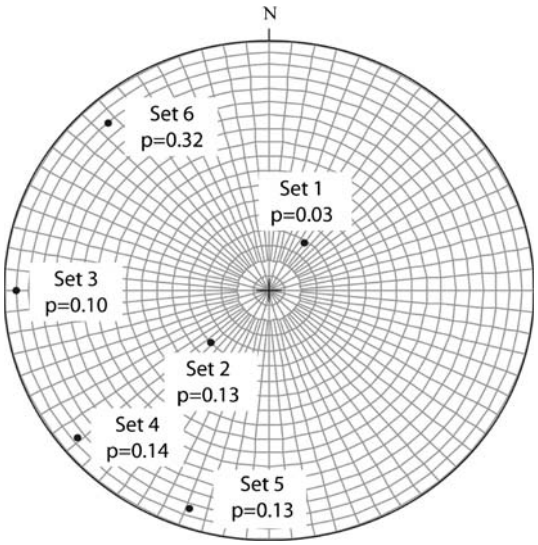

Fig. 10 Lower-hemisphere equal area projection of the poles to the mean orientation vectors for Sets 1 through 6; the remaining 15% of fractures are randomly oriented

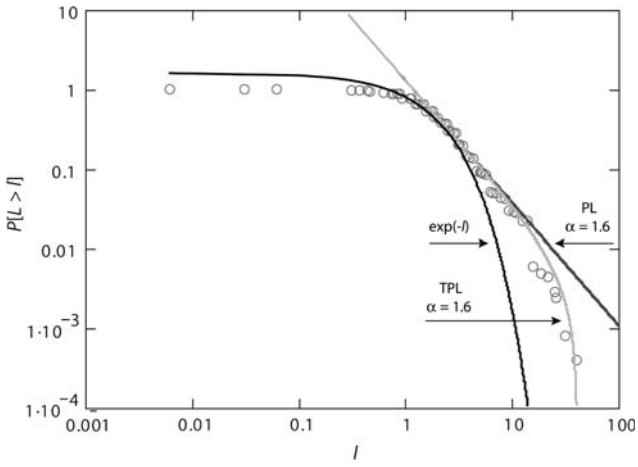

Fig. 11 Mandelbrot plot of all fracture lengths (l along with best fit Pareto power-law (PL), truncated Pareto power-law (TPL) and exponential (exp) models). Note the decay of the largest fracture lengths (i.e., distributional tail) follows a strong power-law trend (linear in log-log space) with an abrupt truncation. The truncation is artificial and results from the length and orientation of the drifts. All fracture lengths are in meters

fractures cluster around a mean orientation is proportional to values of κ (i.e., higher values of κ describe higher degrees of clustering). Values of κ for natural rock fractures range between 10 and 300 (Kemeny and Post 2003). Stochastic simulation of Fisher random deviates is based on a method by Wood (1994). The occurrence of each fracture set is governed by the prior probabilities listed in Table 3. The distribution of fracture orientation for Set 7 is assumed uniform.

Fracture length

Fracture length is perhaps the most important parameter for discrete fracture network investigations. The distribution of fracture length has been found in theoretical studies to control both network connectivity (Renshaw 1999; de Dreuzy 2001) and the spreading rate of solutes at the leading plume edge (Reeves et al. 2008b, c). For the Climax stock, fracture length is recorded for approximately 95% of the fractures contained in the SFT-C data base. Fracture lengths range from 0.006 to 40 m within this data set. The upper range in the data is misleading as fracture length values are restricted to drift length and orientation, i.e., the longest fracture is parallel to one of the drifts and approximately two-thirds of the total drift length (67 m). According to a maximum likelihood estimation method (Aban et al. 2006), fracture length data fit a Pareto power-law distribution ($\alpha = 1.6$) that is truncated for the largest values (denoted as "TPL") (Fig. 11). Again, the truncation in fracture length is artificial, and is a result of the drift orientation and length relative to the occurrence and orientation of fractures.

To honor the power-law trend observed for the fracture length data set (linear trend on Fig. 11), an upper truncated Pareto model is used to randomly assign fracture lengths (Aban et al. 2006):

$$P(L > l) = \frac{\gamma^{\alpha}(l^{-\alpha} - v^{-\alpha})}{1 - (\frac{\gamma}{v})^{\alpha}} \tag{8}$$

where $L_{(1)}, L_{(2)}, \ldots, L_{(n)}$ are fracture lengths in descending order and $L_{(1)}$ and $L_{(n)}$ represent the largest and smallest fracture lengths, γ and v are lower and upper fracture length cutoff values, and α describes the tail of the distribution. Specific values used to describe fracture lengths at the Climax stock include: $\alpha = 1.6$, $\gamma = 30$ m, and $v = 1{,}000$ m. The lower cutoff of 30 m is equal to two times the edge of a cell in the continuum grid (15 m) and the upper cutoff of 1,000 m is equal to one-third of the FCM domain in the x-direction. The purpose of assigning fracture length according to (8) is to restrict fracture length to a finite upper bound. There is no evidence, with the exception of kilometer-scale faults that bound the Climax stock, of large faults that potentially span the entire length ($\sim$5 km) of the stock. Thus, we deem a classical Pareto power-law (denoted as "PL" in Fig. 11) as an inappropriate choice for fracture length.

Fracture density

It is not possible to directly measure the three-dimensional fracture density of a rock mass. Instead, three-dimensional density of discrete fracture networks is estimated from density measures of lower dimensions, i.e., one-dimensional fracture frequency from boreholes or tunnel drifts or

two-dimensional density from outcrops or fracture trace maps. Fracture frequency in the SFT-C database, based on fracture mapping along tunnel drifts, is relatively high and ranges between 2.0 to 5.5 fractures per meter. However, the high fracture spacing in the SFT-C database is misleading as the frequency of "flowing" or conductive fractures is not considered.

Field observations for fractured rock masses indicate that rock volumes are often intersected by only a few dominant fractures and only approximately 10% (or less) of the total fracture population contributes to flow (Dershowitz et al. 2000). This implies that 90% of fractures in the SFT-C database are not connected to the hydraulic backbone. Two specific studies at Climax provide some insight into the frequency of open fractures. In a tunnel drift for the SFT-C experiments, a series of five boreholes extending 9 to 12 meters below the tunnel drift yielded permeability values typical of unfractured granite cores (Ballou 1979). This indicates that the borehole array, which is on the scale of a grid cell, only intersects either solid rock or rock with "healed" fractures. "Healed" fractures (i.e., veins) refer to fractures containing mineral precipitates (e.g., calcite) and are, therefore, not open to flow. Several instances of healed fractures were documented in the SFT-C database by Yow (1984)—these fractures were excluded from the frequency analysis when recorded. In the permeability test conducted by Isherwood et al. (1982), only 2 out of 10 (20%) fractures in a densely fractured zone were open and had permeability values higher than the background matrix.

Given the high level of uncertainty in fracture density, this parameter is determined in the fracture continuum model during calibration (Table 1). Refer to Sect. 3.2 for additional discussion.

Hydraulic conductivity

Only a handful of field-scale hydraulic conductivity (K) measurements exist for the Climax stock (on the order of 10^{-7} to 10^{-10} m/s) (Murray 1980, 1981). These values describe the bulk hydraulic conductivity of the fractured stock, and most likely underestimate variability in fracture K since these estimates are based on hydraulic testing over large open borehole intervals where properties of multiple fractures are averaged. This narrow range (3 orders of magnitude) is inconsistent with other studies of highly characterized fractured granite rock masses where values of fracture K encompass 5–8 orders of magnitude (Paillet 1998; Guimerà and Carrera 2000; Andersson et al. 2002; Hendricks Franssen and Gómez-Hernández 2002; Gustafson and Fransson 2005).

Instead of relying on a handful of effective permeability measurements to parameterize a probability distribution for fracture K, the distribution of mechanical fracture apertures in the SFT-C database is analyzed. Recorded aperture values are lognormally distributed with a standard deviation of 1.05 (not shown) and this value is used to describe the variability in the fracture K distributions. This value is identical to the standard deviation of the transmissivity distribution used by Stigsson et al. (2001) at the Äspö Hard Rock Laboratory. Though rock fracture hydraulic conductivity is proportional to mechanical aperture, correlations between mechanical and equivalent hydraulic apertures are often unreliable (Bandis et al. 1985; Cook et al. 1990); therefore, mean values of K are not computed from the mechanical aperture distribution. Aperture data are used only to gauge the suitability of a lognormal distribution for fracture K and to provide an estimate of standard deviation.

To maintain a constant conceptual model for radionuclide flux estimates (refer to Sect. 3.2 for more detail), fracture K distributions were held constant at values of -7 and -8 (the original values of K are in units of meters per second prior to log transformation). Both of these mean fracture K values are within the narrow range defined by Murray (1981). The higher mean value of -7 m/s is assigned to fractures that belong to fracture set 6 (32% of the fractures) (Table 3). Fractures in this set experience the least amount of compressive stress normal to their fracture walls, suggesting that these fractures are potentially more permeable than fractures oriented at other directions to the regional stress field. The remaining fracture sets (68% of the fractures) are assigned K values according to the lower mean K of -8. A $\log_{10}$ K standard deviation value of 1.05 is applied to all fracture sets.

Fracture porosity

The computation of cell velocity from Darcy flux values calculated in the FCM flow realizations requires values of fracture and matrix cell porosity. Constant values of 0.006 are assigned to matrix cells (Murray 1981). Equivalent porosity values of fracture cells are based on tracer test results from a similar fractured granite rock mass where equivalent porosity was found to be lognormally distributed within a range of 0.027 and 0.054 (Pohlmann et al. 2004). Given the hydraulic conductivity distribution for fractures at Climax, an empirical power-law relationship:

$$n = 0.04(K_{\text{fracture}})^{0.25} \tag{9}$$

is used to correlate fracture cell porosity n with fracture hydraulic conductivity K_{fracture}, while maintaining both the range and distribution of the porosity values reported by Pohlmann (2004).

References

Aban IB, Meerschaert MM, Panorska AK (2006) Parameter estimation methods for the truncated Pareto distribution. J Amer Stat Assoc 101:270–277

Akaike H (1974) A new look at statistical mdoel identification. IEEE Trans Automat Contr AC-19:716–722

Andersson J, Dershowitz B, Hermanson J, Meier P, Tullborg E-L, Winberg A (2002) Final report of the TRUE block scale project. 1. Characterization and model development, TR-02-13. Swedish Nuclear Fuel and Waste Management Co. (SKB), Stockholm, Sweden

Ballou L (1979) Field permeability measurements, Waste Isolation Projects: FY 1978, UCRL-50050-78. Lawerence Livermore National Laboratory, Livermore, California

Bandis SC, Makurat A, Vik G (1985) Predicted and measured hydraulic conductivity of rock joints. In: Proceedings of the international symposium on fundamentals of rock joints, Björdkliden, Norway, September 15–20

Bechtel Nevada (2006) A hydrostratigraphic model and alternatives for the groundwater flow and contaminant transport model of Corrective Action Unit 97: Yucca Flat-Climax Mine, Lincoln and Nye Counties, Nevada, DOE/NV/11718-1119

Belcher WR (ed) (2004) Death Valley regional ground-water flow system, Nevada and California—hydrgeologic framework and transient ground-water flow model. U.S. Geological Survey Scientific Investigations Report 2004–5205

Belcher WR, D'Agnese FA, O'Brien GM (2004) Introduction, Chapter A. In: Belcher WR (ed) Death Valley regional ground-water flow system, Nevada and California—hydrgeologic framework and transient ground-water flow model. U.S. Geological Survey Scientific Investigations Report 2004–5205

Beven KJ, Binley AM (1992) The future of distributed models: model calibration and uncertainty prediction. Hydrol Process 6:279–298. doi:10.1002/hyp.3360060305

Beven KJ, Freer J (2001) Equifinality, data assimilation, and uncertainty estimation in mechanistic modeling of complex environmental systems using the GLUE methodology. Hydrol. Process 6:279–298

Botros F, Hassan AE, Reeves DM, Pohll G (2008) On mapping fracture networks onto continuum. Water Resour Res 44:WO8435. doi:10.1029/2007WR006092

Bowen S, Finnegan DL, Thompson JL, Miller CM, Baca PL, Olivaas LF, Goffrion CG, Smith DK, Goishi W, Esser BK, Meadows JW, Namboodiri N, Wild JF (2001) Nevada Test Site radionuclide inventory 1951–1992, LA-13859-MS. Los Alamos National Laboratory, Los Alamos, New Mexico

Cook AM, Myer LR, Cook NGW, Doyle FM (1990) The effect of toruosity on flow through a natural fracture, Rock mecdhanics contributions and challenges. In: Hustrulid WA, Johnson GA (eds) Proceedings of the 31st U.S. symposium on rock mechanics. A.A. Balkema, Rotterdam

de Dreuzy J-R, Davy P, Bour O (2001) Hydraulic properties of two-dimensional random fracture networks follwoing a power law length distribution. 1. Effective connectivity. Water Resour Res 37(8)2065–2078

Dershowitz WJ, Hermanson S, Follin S, Mauldon M (2000) Fracture intensity measures in 1-D, 2-D, and 3-D at Äspö, Sweden. In: Proceedings of the fourth North American rock mechanics symposium, Pacific Rocks 2000, vol 4, Seattle, Washington, pp 849–853

Doherty J (2000) PEST—model-independent parameter estimation—user's manual, 4th edn. Watermark Numerical Computing

Faure G (1977) Principles of isotope geology. John Wiley and Sons, New York

Federal Facility Agreement and Consent Order (1996, as amended) Agreed to by the State of Nevada, the U.S. Department of Energy, and the U.S. Department of Defense

Fisher R (1953) Dispersion on a sphere. Proc R Soc Lond Ser A 217:295–305

Franks SW, Beven KJ, Gash JHC (1999) Multi-objective conditioning of a simple SVAT model. Hydrol Earth Syst Sci 4:477–789

Guimerà J, Carrera J (2000) A comparison of hydrualic and transport parameters measured in low-permeability fractured media. J Contam Hydrol 41:261–281

Gustafson G, Fransson A (2005) The use of the Pareto distribution for fracture transmissivity assessment. Hydrogeol J. doi:10.1007/s10040-005-0440-y

Harbaugh AW, Banta ER, Hill MC, McDonald MG (2000) MODFLOW-2000, the U.S. Geological Survey Modular Ground-Water Model—user guide to modularization concepts and the ground-water flow process. U.S. Geological Survey Open–File Report 00-92

Hassan AE, Mohamed MM (2003) On using particle tracking methods to simulate transport in single-continuum and dual continua porous media. J Hydrol 275:242–260

Hendricks Franssen HJWM, Gómez-Hernández JJ (2002) 3D inverse modelling of groundwater flow at a fractured site using a stochastic continuum model with multiple statistical populations. Stoch Environ Res Risk Assess 16:155–174. doi:10.1007/s00477-002-0091-7

Hurvich CM, Tsai C-L (1989) Regression and time series model selection in small sample, Biometrtika 76:99–104

Isherwood D, Harrar J, Raber E (1982) Characterization of Climax granite ground water, UCRL-53309. Lawrence Livermore National Laboratory, Livermore, CA

Kashyap RL (1982) Optimal choice of AR and MA parts in autoregressive moving models. IEEE Trans Pattern Anal Mach Intell 4:99–104

Kemeny J, Post R (2003) Estimating three-dimensional rock discontinuity orientation from digitial images of fracture traces. Comput Geosci 29:65–77

LaBolle E, Fogg G, Thompson AFB (1996) Random-walk simulation of solute transport in heterogeneous porous media: local mass-conservation and implementation methods. Water Resour Res 32:583–593

LaBolle E, Quastel J, Fogg G, Gravner J (2000) Diffusion processes in composite porous media with their integration by numerical walks: generalizated stochastic differential equations with discontinuous coefficients. Water Resour Res 36:651–662

Liu HH, Bodvarsson GS, Pan L (2000) Determination of particle transfer in random walk methods for fractured porous media. Water Resour Res 36:707–713

Mardia KV, Jupp PE (2000) Directional statistics. Wiley, New York

Munier R (2004) Statistical analysis of fracture data adopted for modeling discrete fracture networks—version 2. Rep. R 04-66. Swedish Nuclear Fuel and Waste Management, Co. (SKB). Stockholm, Sweden

Murray WA (1980) Permeability testing of fractures in Climax stock granite, NTS. In: Repository sealilng field testing workshop, Santa Fe, New Mexico, September 18–19

Murray WA (1981) Geohydrology of the Climax stock granite and surrounding rock formations, NTS, UCRL-53138. Lawrence Livermore National Laboratory, Livermore, CA

Neuman SP (2003) Maximum likelihood Bayesian averaging of uncertain model predictions. Stoch Environ Res Risk Assess 17:291–305. doi:10.1007/s00477-003-0151-7

Paillet FL (1988) Flow modeling and peremability estimation using borehole flow logs in heterogeneous fractured formations. Water Resour Res 34(5):997–1010

Pohlmann K, Pohll G, Chapman J, Hassan AE, Carroll R, Shirley C (2004) Modeling to support groundwater contaminant boundaries for the Shoal underground nuclear test. Desert Research Institute, Division of Hydrologic Sciences Publication No. 45184

Pohlmann K, Ye M, Reeves D, Zavarin M, Decker D, Chapman J (2007) Modeling of groundwater flow and radionuclide transport at the Climax mine sub-CAU, Nevada Test Site, DOE/NV/26383-06. Nevada Site Office, National Nuclear Security Administration, U.S. Department of Energy, Las Vegas, NV

Reeves DM, Benson DA, Meerschaert MM (2008a) Transport of conservative solutes in simulated fracture networks. 1. Synthethic data generation. Water Resour Res 44:W05401. doi:10.1029/2007WR006069

Reeves DM, Benson DA, Meerschaert MM, Scheffler H-P (2008b) Transport of conservative solutes in simulated fracture networks. 2. Ensemble solute transport and the correspondence to operator-stable limit distributions. Water Resour Res 44:W05410. doi:10.1029/2008WR006858

Reeves DM, Benson DA, Meerschaert MM (2008c) Influence of fracture statistics on advective transport and implications for geologic repositories. Water Resour Res 44:W08405. doi:10.1029/2007WR006179

Renshaw CE (1999) Connectivity of joint networks with power law length distributions. Water Resour Res 35(9):2661–2670

Russell CE, Minor T (2002) Reconnaissance estimates of recharge based on an elevation-dependent cloride mass-balance approach, DOE/NV11508-37. Nevada Site Office, National Nuclear Security Administration, U.S. Department of Energy, Las Vegas, NV

Schwarz G (1978) Estimating the dimension of a model. Annu Stat 6(2):461–464

Stigsson M, Outters N, Hermanson J (2001) Äspö Hard Rock Laboratory, Prototype repository hydraulic DFN model no. 2, IPR-01-39. Swedish Nuclear Fuel and Waste Management Co. (SKB), Stockholm, Sweden

U.S. Department of Energy (DOE) (2000a) United States Nuclear Tests, July 1945 through September 1992, DOE/NV-209 (Rev. 15). Nevada Operations Office

U.S. Department of Energy (DOE) (2000b) Investigation Plan for Corrective Action Unit 97: Yucca Flat/Climax Mine, Nevada Test Site, Nevada. DOE/NV-659. Nevada Operations Office

Vrugt JA, ter Braak CJF, Gupta HV, Robinson BA (2008) Equifinality of formal (DREAM) and informal (GLUE) Bayesian approaches in hydrologic modeling. Stoch Environ Res Risk Assess. doi:10.1007/s00477-008-0274-y

Wood ATA (1994) Simulation of the Von Mises distribution. Commun Stat-Sim 23(1):157–164

Ye M, Pohlmann KF, Chapman JB (2008) Expert elicitation of recharge model probabilities for the Death Valley regional flow system. J Hydrol 354:102–115. doi:10.1016/j.jhydrol.2008.03.001

Ye M, Pohlmann KF, Chapman JB, Pohll GM, Reeves DM (2010) A model-averaging method for assessing groundwater conceptual model uncertainty. Ground Water. doi:10.1111/j.1745-6584.2009.00633.x

Yow JL (1984) Geologic structure mapping database, Spend Fuel Test—Climax, Nevada Test Site, DE85006267